Entanglement between muon and $I > \frac{1}{2}$ nuclear spins as a probe of charge environment - Supplemental Material

Pietro Bonfà,[1,*] Jonathan Frassineti,[2] John M. Wilkinson,[3] Giacomo Prando,[4] Muhammad Maikudi Isah,[1] Chennan Wang,[5] Tiziana Spina,[6] Boby Joseph,[7] Vesna F. Mitrović,[8] Roberto De Renzi,[1] Stephen J. Blundell,[3] and Samuele Sanna[2]

[1] *Department of Mathematical, Physical and Computer Sciences, University of Parma, Italy*
[2] *Department of Physics and Astronomy, University of Bologna, Italy*
[3] *Clarendon Laboratory, Department of Physics, University of Oxford, Parks Road, Oxford OX1 3PU, United Kingdom*
[4] *Department of Physics, University of Pavia, Italy*
[5] *Laboratory for Muon Spin Spectroscopy, Paul Scherrer Institute, CH-5232 Villigen, Switzerland*
[6] *Superconducting Radio Frequency (SRF) Materials and Research Department, Fermilab, Batavia, USA*
[7] *Elettra-Sincrotrone Trieste, S.S. 14-km 163.5, Basovizza, 34149 Trieste, Italy*
[8] *Department of Physics, Brown University, Providence, 02912 Rhode Island, USA*

(Dated: July 13, 2022)

I. EXPERIMENTAL DETAILS

A. Sample preparation

V_3Si and V_3Sn powder samples have been prepared at the Institut NEEL – CNRS in Grenoble (France) by using starting bulk elements, minimum 5N purity, weighted in stoichiometric ratio and melted using a copper cold crucible under high frequency and high purity argon atmosphere. Depending on their different chemical phase diagrams, the heat treatments were direct melt for V_3Si and melt plus annealing for V_3Sn. The as-cast V_3Sn sample has been wrapped in a titanium foil, sealed in a quartz tube under high vacuum and heated at 950°C during 32 days.

Tiny Nb_3Sn samples were fabricated starting from a polycrystalline bulk piece sintered by Hot Isostatic Pressure (HIP) technique (2 kbar Argon pressure at 1250 °C for 24h) at the University of Geneva [1]. This Nb_3Sn bulk piece was cut into small platelets by spark erosion and then polished with SiC grinding papers. To remove stresses induced by the polishing procedure, a "flash-anneal" heat treatment (900 °C/10 min) was applied. From SEM/EDS analysis the grain size of ~ 20 μm and a composition very close to stoichiometry (24.8 at. % Sn) has been determined. Further details on the procedure and analysis can be found in ref. [2–5].

B. X-rays diffraction characterization

Synchrotron x-ray powder diffraction measurements have been performed at the ELETTRA synchrotron Facility in Trieste (Italy). V_3Si and V_3Sn samples were measured at the XRD1 beamline using wavelength 0.7 Å whereas Nb_3Sn was measured at the Xpress beamline using wavelength 0.4957 Å.

Rietveld refinements were made by using GSAS-II software and aimed mainly to check phase purity and to determine the lattice parameters, necessary as input parameters for the simulation of the muon polarization (see below).

Representative diffraction patterns measured at room temperature are displayed in Fig. 1 with their Rietveld fit curves. All the samples have a A15 cubic structure with the $Pm\bar{3}n$, group number 223, symmetry and display lattice parameters a =4.7226(2) Å, 4.981 86(2) Å, 5.288 68(2) Å for V_3Si, V_3Sn and Nb_3Sn respectively, in agreement with previous results [2, 3, 6, 7]. Unlike V_3Si and Nb_3Sn, in case of V_3Sn we observed several minor impurity phases which were identified to be due to different oxide phases of V and Sn (about 3-5 %) and an additional 5 % contribution of the hexagonal V_3Sn phase. Since these phases are segregated and the μSR measurements give a bulk response, proportional to the relative volume phase, the results of this work are not affected by a small fraction of spurious phases.

* pietro.bonfa@unipr.it

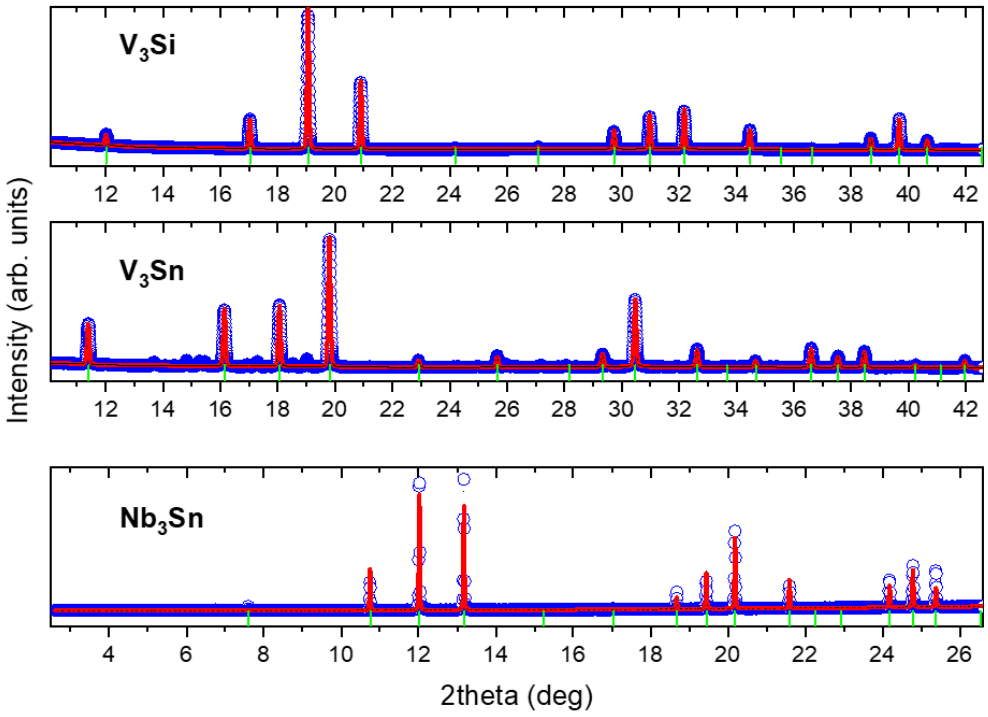

(a)

FIG. 1. X-ray diffraction patterns for V_3Si, V_3Sn, and Nb_3Sn, at T = 300 K. The blue points are the experimental data, the red lines the Rietveld refinement fits and the green ticks represent the Bragg reflections of the A15 cubic structure with the $Pm\bar{3}n$, group number 223.

C. Muon spin spectroscopy experiments

Our experiments were performed using the EMU spectrometer at the pulsed beam ISIS Facility, Rutherford Appleton Laboratory, UK, and GPS spectrometer at the continuous beam Swiss Muon Source SμS, Paul Scherrer Institute, Villigen, Switzerland. The first allows to collect a high statistics, thanks to high data rate acquisition of time-differential data at pulsed sources, but is typically affected by a large background due to muons implanting in the sample holder or in the wall of the cryostat. On the other hand, the second allows to nearly eliminate the background signal thanks to the smaller beam size and to the use of the VETO option. In our case the combination of the two is essential in order to collect data acquisition much higher than the muon lifetime (τ = 2.2 microseconds), to resolve possible long-time features of the μSR signal, and to properly subtract the background for a more accurate comparison with the DFT simulations. All the powder samples were measured with the GPS spectrometer while V_3Sn and V_3Si were also measured with the EMU instrument, with high statistic for some selected temperatures. The powders were wrapped in sheet of 25 μm silver foil, and were placed in the cryostat and measured in the range 20-300 K and in zero external magnetic field conditions. The Earth's magnetic field was compensated to better than 50 μT using active field compensation.

In the muon experiment, a beam of spin-polarized muons were implanted into a sample, and the number of positrons emitted in both the forwards and backwards detectors, $N_F(t)$ and $N_B(t)$ respectively, was measured. The muon spin polarization was calculated as $P(t) = A(t)/A_0$ being $A(t)$ the time dependent muon decay asymmetry and A_0 its initial value $A(0)$. The muon asymmetry is determined as $A(t) = (N_B(t) - \alpha N_F(t))/(N_B(t) + \alpha N_F(t))$ where the parameter α takes into account systematic differences between the readings of both sets of detectors. Both α and A_0 were properly calibrated at high temperature by applying a small transverse field (of few mT).

The background component of ISIS measurements has been estimated by comparing them with the acquisitions performed at PSI at the lowest temperature. The data are linearly interpolated on the same time intervals. Finally, the constant shift providing the best overlap among the two curves is estimated and subtracted from the ISIS measurements.

II. COMPUTATIONAL RESULTS

Density Functional based simulations have been performed using a plane wave (PW) basis with the Quantum ESPRESSO code, and with Augmented Plane Waves using the Full Potential (FP) code Elk [8, 9]. In all simulations we used the PBE exchange and correlation functional [10].

In PW based simulations the maximum k-point distance was 0.2 Å^{-1}, obtained using a Γ centered $4 \times 4 \times 4$ grid for the $2 \times 2 \times 2$ supercells and with a Γ centered $2 \times 2 \times 2$ grid for the $3 \times 3 \times 3$ supercells. A Marzari-Vanderbilt smearing with 5 mRy width was used. We chose ultrasoft pseudopotentials [11] for lattice structure relaxation, and PAW potentials [12] for estimating electric field gradients (EFG) at the various nuclear sites. A cutoff of 60 (600) Ry was used for wavefunction (charge) cutoffs. The experimental lattice parameters of the cubic structure were always enforced.

FP simulations were performed with the high quality setting for the description of the basis (refer to Elk's manual for further details), but carefully defining muffin tin radii to allow the simulation of the interstital H atom. The maximum k-point distance in the grid was smaller than 0.4 Å^{-1} in this case (with Γ centered $8 \times 8 \times 8$ grids for the unit cells, and Γ centered $2 \times 2 \times 2$ for the supercells). All input files and relevant output files to reproduce our results are available on materialscloud [13].

A. Muon sites

The muon sites were found by relaxing the atomic positions of $2 \times 2 \times 2$ supercells (SC) where an interstitial hydrogen atom was placed in 5 interstitial positions obtained considering the symmetry inequivalent points of a $4 \times 4 \times 4$ grid of initial sites. An overall neutral charge state has been considered since, in a metallic ground state, the positively charged muon is screened by conduction electrons. We have indeed verified that the positively charged supercell with a constant compensating background yields the same muon sites in V_3Si.

Two interstitial positions are always obtained and shown with letters A and B in Fig. 2 where X is either V or Nb and Y is Si or Sn. Position A is at the center of the tetrahedron formed by 4 X atoms while position B is at the centre of the triangles formed by 3 X atoms.

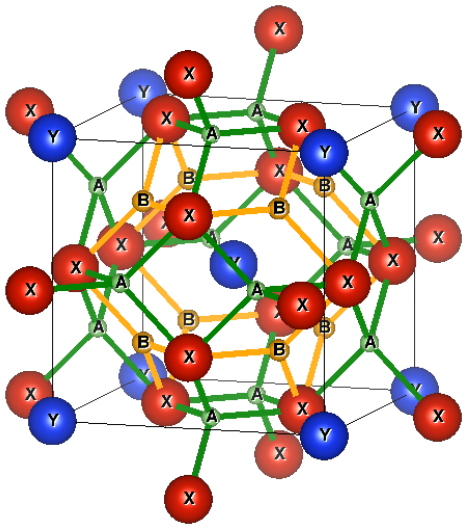

FIG. 2. Candidate muon sites in A15 compounds. Letters A and B identify the two stable interstitial positions while X is V or Nb and Y is Si or Sn in V_3Si, V_3Sn, and Nb_3Sn.

The results for the A site, always found to be the lowest energy site, were further refined with the structural relaxation of a muon directly placed in site A in a $3 \times 3 \times 3$ SC. This also allowed to verify the convergence against the SC size. The outcomes of the simulations are reported in Table I.

Finally, in light of the lower quality of the V_3Sn sample, we also explored the possibility that V and/or Sn vacancies may trap the muon [14–16]. The interstitial positions for a muon in a vacancy site has been explored by obtaining the embedding muon position after initially placing it in place of the vacant V or Sn atom in a $2 \times 2 \times 2$ supercell (with a small displacement of the initial position to remove the symmetry constraints on atomic forces). The optimized

TABLE I. Properties of the muon sites in A15 compounds.

Sample	$d^{(A)}_{X-\mu}$ (Å) from $2\times2\times2$ SC	$d^{(A)}_{X-\mu}$ (Å) from $3\times3\times3$ SC	$d^{(B)}_{X-\mu}$ (Å)	$E_B - E_A$ (meV)
V_3Si	1.75	1.76	1.74	350
V_3Sn	1.84	1.85	1.76	530
Nb_3Sn	1.95	1.96	1.89	330

position of all atoms and the EFG at the neighbouring V atoms are used to perform the same analysis described in the main text. The seven V neighbours residing inside a sphere of $r = 3$ Å from the muon were considered for the Sn vacancy site while the same number of V neighbours resides inside a $r = 3.6$ Å sphere for the V vacancy site. The contribution from the remaining nuclei of the system is neglected (see next section for the details). The simulation of the muon asymmetry in these centers shows worse agreement with the experimental data as displayed in Fig 3.

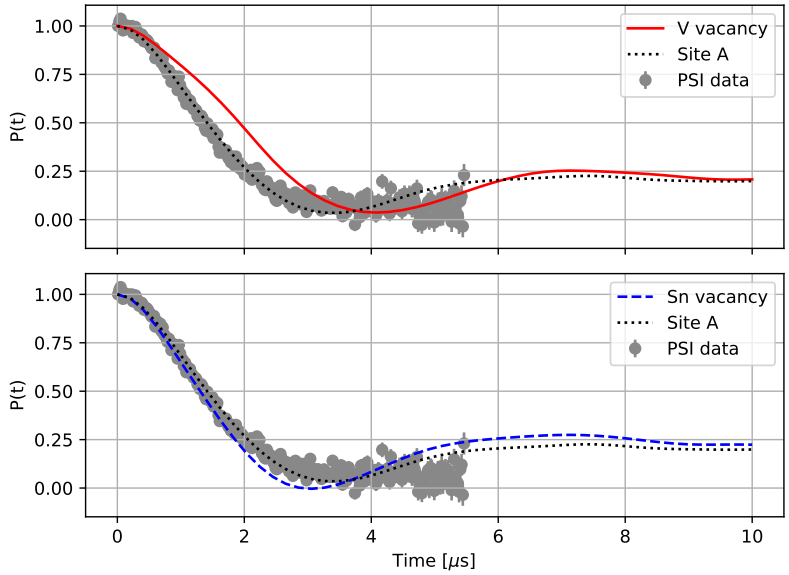

FIG. 3. Polarization function obtained for V and Sn vacancy sites in V_3Sn compared with the interstitial site A and the experimental data obtained at PSI at 23 K.

B. Muon spin simulations

The muon spin polarization was numerically evaluated with the approach proposed by Celio and implemented in UNDI [17–19]. The method must be converged against the Trotter expansion and, more importantly, the number of random initial states used to describe the nuclei. The time step in the evolution of the wavefunction was set to 100 ns. When considering four nearest neighbors, the results converge to better than experimental accuracy with 4 repetitions, while, when performing simulations with 4 nn and 4 nnn, a single repetition was found to be sufficient. The electric field gradient obtained *ab initio* is applied to all quadrupolar nuclei.

As the Hilbert space grows exponentially with the number of spins considered in the calculation, the inclusion of the dipolar interactions between the muon and the nuclei beyond the nnns was achieved by re-scaling the distance between them and the muon, in a procedure similar to [20]. These rescaling factors were calculated by considering the second moment of the dipolar field distribution at the muon site, which for M spins is

$$\sigma_M^2 = \frac{2}{3}\left(\frac{\mu_0}{4\pi}\right)^2 \hbar^2 \gamma_\mu^2 \sum_{j=1}^{M} \frac{\gamma_j^2 I_j(I_j+1)}{r_j^6}, \tag{1}$$

where r_j is the distance from the muon to the j^{th} nucleus with spin I_j and gyromagnetic ratio γ_j, $\gamma_\mu (= 2\pi \times$

135.5 MHz T^{-1}) is the muon gyromagnetic ratio, and the sum converges as $M \to \infty$. We then calculate $\zeta_{\rm nnn}$ from

$$\sigma_\infty^2 = \sigma_{\rm nn}^2 + \frac{2}{3}\left(\frac{\mu_0}{4\pi}\right)^2 \hbar^2 \gamma_\mu^2 \sum_{j \in {\rm nnn}} \frac{\gamma_j^2 I_j (I_j+1)}{(\zeta_{\rm nnn} r_j)^6}, \tag{2}$$

and then evaluate the calculation of the dipolar terms in the Hamiltonian to the restricted set of spins comprising the muon, the nn and the nnn nuclei (with the distance between the ion and the muon rescaled by $\zeta_{\rm nnn}$). In particular, $\zeta_{\rm nnn}$ was calculated as 0.8150, 0.7981, 0.8106 for V_3Si, V_3Sn, Nb_3Sn respectively. This marginally affects the depolarization in most of the cases discussed in the main text, but the effect is meaningful when compared to the experimental uncertainty, as shown for example for V_3Si in Fig. 4.

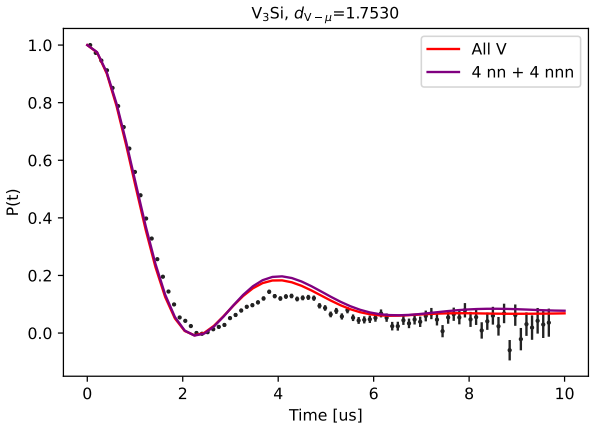

FIG. 4. Predicted μ^+ depolarization obtained considering 4 nn and 4 nnn vanadium nuclei (purple line) and effectively considering all V nuclei (red line) in V_3Si. The black points are experimental results (see main text for details).

These simulations are instead very sensitive to the electric field gradient at V or Nb sites and further details are reported in the next section.

C. Electric Field Gradients

In order to obtain the perturbed EFG at the X sites, we performed both FP and PW based simulations using, in addition to previously mentioned programs, the GPIAW code [21]. The EFG tensors were acquired in relaxed $3\times3\times3$ SC when using PW while it was impossible to run the same simulations with the FP method. For this reason we collected the estimate using $2\times2\times2$ SC imposing the displacement obtained from $3\times3\times3$ PW simulations only to the nearest neighbours to the muon. As shown in Fig. 3 in the main paper, this isn't a drastic approximation since lattice distortions decay quickly.

The results for the pristine materials are reported in the first two columns of Tab. II while V_{zz} of the nearest X atoms of the muon are shown in the last two columns. As already shown in the main text, small variations of the EFG at X sites can be appreciated in the prediction of the muon polarization. The small difference between FP and PW results for V_3Sn is enough to significantly improve the agreement with the experimental data, as shown in the main text.

TABLE II. EFGs at X sites. The results are reported in atomic units (1 a.u. = 9.71736×10^{21} Vm^{-2}) as produced by Elk and GIPAW. The first two columns are the results for the unperturbed materials while the last two are for the nn of the muon.

Sample	V_{zz} for Bulk (FP)	V_{zz} Bulk PW	Perturbed V_{zz} on nn, FP	Perturbed V_{zz} on nn, PW
V_3Si	-0.21	-0.23	-0.043	-0.0422
V_3Sn	0.12	0.16	0.21	0.24
Nb_3Sn	0.47	0.42	-	-0.13

A careful analysis of the effect of small variations of EFG and $d_{X-\mu}$ has been made for V_3Si. Fig. 5 shows the depolarization obtained as a function of the distance between the muon and V nuclei. A FP simulation has been

performed for each $\mu - V$ separation shown in the legend and the EFG reevaluated. Perfect agreement is found for a displacement only 15 mÅ larger than the one obtained with the full relaxation of a $3 \times 3 \times 3$ SC performed with the PW basis.

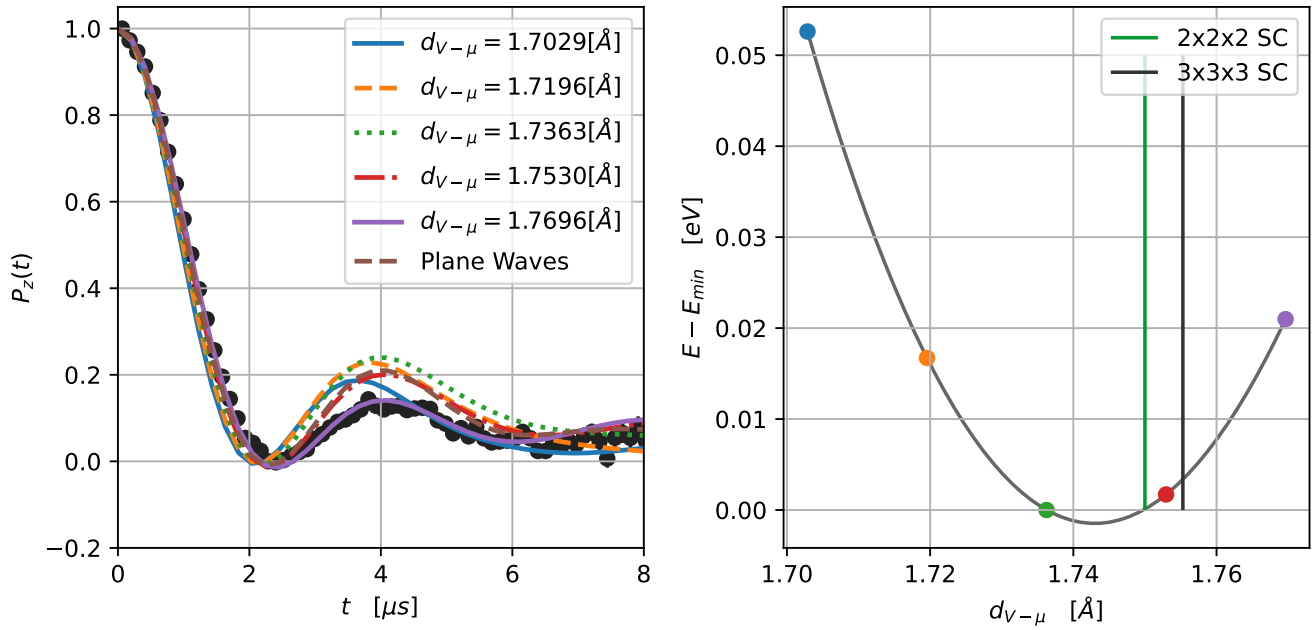

FIG. 5. Left: comparison of FP results for various μ−V separations obtained by displacing the position of nearest neighbouring V atoms radially to obtain the separation shown in the label. The brown dashed line is the fully *ab initio* result obtained with PW. Right: energy vs μ−V distance in FP simulations. The vertical green and black lines show the equilibrium distance found with a full relaxation of the lattice in $2 \times 2 \times 2$ and $3 \times 3 \times 3$ SC simulations performed with a PW basis set. The gray line is an interpolation between the coloured points obtained with FP simulations in a $2 \times 2 \times 2$ SC where only the 4 nearest neighbors of the muon are displaced from equilibrium positions. The small discrepancy between the equilibrium distance that can be obtained from the minimum of the curve interpolating FP results and the $2 \times 2 \times 2$ PW result (green vertical line) is due to the absence of shifts from equilibrium positions of all atoms but nn of the muon. This incidentally shows that this second order effect is very small.

[1] T. Spina, *Proton Irradiation Effects on Nb_3Sn Wires and Thin Platelets in View of High Luminosity LHC Upgrade*, Ph.D. thesis, Deparement de Physique de la Matiere Quantique (DQMP), Universite de Geneve (2015).

[2] R. Flükiger, T. Spina, F. Cerutti, A. Ballarino, C. Scheuerlein, L. Bottura, Y. Zubavichus, A. Ryazanov, R. D. Svetogovov, S. Shavkin, P. Degtyarenko, Y. Semenov, C. Senatore, and R. Cerny, Variation of T_c, lattice parameter and atomic ordering in Nb_3Sn platelets irradiated with 12 MeV protons: correlation with the number of induced Frenkel defects, Superconductor Science and Technology **30**, 054003 (2017).

[3] A. Alimenti, N. Pompeo, K. Torokhtii, T. Spina, R. Flükiger, L. Muzzi, and E. Silva, Microwave measurements of the high magnetic field vortex motion pinning parameters in Nb_3Sn, Superconductor Science and Technology **34**, 014003 (2020).

[4] A. Alimenti, N. Pompeo, K. Torokhtii, T. Spina, R. Flk̈iger, L. Muzzi, and E. Silva, Surface Impedance Measurements on Nb_3Sn in High Magnetic Fields, IEEE Trans. Appl. Supercond **29**, 3500104 (2019).

[5] I. Schiesaro, S. Anzellini, R. Loria, R. Torchio, T. Spina, R. Flükiger, T. Irifune, E. Silva, and C. Meneghini, Anomalous Behavior in the Atomic Structure of Nb_3Sn under High Pressure, Crystals **11**, 10.3390/cryst11040331 (2021).

[6] C. Paduani and C. A. Kuhnen, Martensitic phase transition from cubic to tetragonal V_3Si: an electronic structure study, Eur. Phys. J. B **66**, 353 (2008).

[7] N. Morton, B. James, G. Wostenholm, and N. Howard, The resistivity of V_3Sn and related compounds, Journal of the Less Common Metals **64**, 69 (1979).

[8] P. Giannozzi, O. Baseggio, P. Bonfà, D. Brunato, R. Car, I. Carnimeo, C. Cavazzoni, S. de Gironcoli, P. Delugas, F. Ferrari Ruffino, A. Ferretti, N. Marzari, I. Timrov, A. Urru, and S. Baroni, Quantum ESPRESSO toward the exascale, The Journal of Chemical Physics **152**, 154105 (2020).

[9] The Elk Code, http://elk.sourceforge.net/.

[10] J. P. Perdew, K. Burke, and M. Ernzerhof, Generalized gradient approximation made simple, Phys. Rev. Lett. **77**, 3865 (1996).

[11] K. F. Garrity, J. W. Bennett, K. M. Rabe, and D. Vanderbilt, Pseudopotentials for high-throughput DFT calculations, Computational Materials Science **81**, 446 (2014).

[12] A. Dal Corso, Pseudopotentials periodic table: From h to pu, Computational Materials Science **95**, 337 (2014).

[13] P. Bonfà, J. Frassineti, J. M. Wilkinson, G. Prando, M. M. Isah, C. Wang, T. Spina, B. Joseph, V. F. Mitrović, R. D. Renzi, S. J. Blundell, and S. Sanna, Entanglement between a muon spin and $I > 1/2$ nuclear spins, https://doi.org/10.24435/materialscloud:7j-vg (2022).

[14] A. Möslang, H. Graf, G. Balzer, E. Recknagel, A. Weidinger, T. Wichert, and R. I. Grynszpan, Muon trapping at monovacancies in iron, Phys. Rev. B **27**, 2674 (1983).

[15] R. Vilão, J. Gil, H. Alberto, J. Duarte, N. de Campos, A. Weidinger, M. Yakushev, and S. Cox, Muon diffusion and trapping in chalcopyrite semiconductors, Physica B: Condensed Matter **326**, 181 (2003).

[16] J. Woerle, T. Prokscha, A. Hallén, and U. Grossner, Interaction of low-energy muons with defect profiles in proton-irradiated si and 4h-sic, Phys. Rev. B **100**, 115202 (2019).

[17] M. Celio, A new technique to calculate the muon polarization function, Hyperf. Inter. **31**, 41 (1986).

[18] M. Celio, New method to calculate the muon polarization function, Phys. Rev. Lett. **56**, 2720 (1986).

[19] P. Bonfà, J. Frassineti, M. M. Isah, I. J. Onuorah, and S. Sanna, Undi: An open-source library to simulate muon-nuclear interactions in solids, Comp. Phys. Comm. **260**, 107719 (2021).

[20] J. M. Wilkinson and S. J. Blundell, Information and decoherence in a muon-fluorine coupled system, Phys. Rev. Lett. **125**, 087201 (2020).

[21] N. Varini, D. Ceresoli, L. Martin-Samos, I. Girotto, and C. Cavazzoni, Enhancement of DFT-calculations at petascale: Nuclear magnetic resonance, hybrid density functional theory and Car–Parrinello calculations, Computer Physics Communications **184**, 1827 (2013).